# ISIMA project : planetesimal formation and shearing instabilities at the dust-rich midplane

J. Masson[a], T. Muto[b], E. I. Chiang[c]

[a] *École normale supérieure de Lyon, CRAL, UMR CNRS 5574, 69364 Lyon Cedex 07, France*
[b] *Department of Earth and Planetary Sciences, Tokyo Institute of Technology, 2-12-1 Oh-okayama, Meguro-ku, Tokyo, 152-8551, Japan*
[c] *UC Berkeley Astronomy, 601 Campbell Hall, Berkeley CA 94720*

**Abstract**

*Keywords:* —planetesimal formation, dust-rich midplane, Kelvin-Helmholtz instability—

## 1. Introduction

### *1.1. General context*

This project takes place in the general framework of planets formation, and more precisely focus on the growth of grains at the dust-rich midplane in protoplanetary disks. There are many scales, and many physical processes at stake in the context of growing grains : from the tiny scales (sub-mm) where chemical bonds and sticking play a major role, to the biggest scales (km to planet-size) which is the domain of gravity. In the intermediate scale (from cm to m or km) sticking is not efficient anymore, and even though the gravity of individual grains is negligible, it is reasonable to try to focus on collective gravitational processes to form bigger grains.

There are two thresholds to cross in order for the gravitational instability to occur in a protoplanetary disk. First, an incompressible fluid at a distance $r$ from a star of mass $M_\star$ can resist the tidal disruption from a star if its density is greater than the Roche value : $\rho \geq \rho_{Roche} = 3.5\frac{M_\star}{r^3}$. This density is 2 to 3 orders of magnitude greater than typical densities in protoplanetary disks, but there is an even more stringent condition for the gravitational instability to occur: the Toomre criteria. The Toomre parameter is a good indication of whether the gravitational instability can occur. It reads:

$$Q = \frac{c\Omega}{\pi G\Sigma} \tag{1}$$

If $Q < 1$, the collapse can occur ! Translated in density values, it gives:

$$\rho_Q \geq 10^{-7}(\frac{r}{a.u.})^{-3}\, g.cm^{-3} \tag{2}$$

$$\rho_{disk} \simeq 2.7 \times 10^{-9}(\frac{r}{a.u.})^{-\frac{39}{14}}\, g.cm^{-3} \tag{3}$$

Is there any means to reach such high densities ? Figure 1 summarizes four mechanisms helping to get denser and denser densities. The tidal gravity perpendicular to the disk enables the settling of dust particules on the equatorial plane (a). The radiation from the star can increase the relative density of the dusty layer compared to the gas (b). It can then be even more concentrated through radial pileup due to the radial Keplerian shear (c), and streaming or drag instabilities (d). [7] and [3] studied these phenomena and concluded those densities *approaching* the density threshold could be attained thanks to these processes (*approaching* meaning still a factor 10 to 20 to go).

Nevertheless, and as pointed out after by [9], as the dust settles in a thiner and thiner (and denser and denser) layer, at some point the turbulence and/or the Kelvin-Helmholtz instability will destroy this layer,

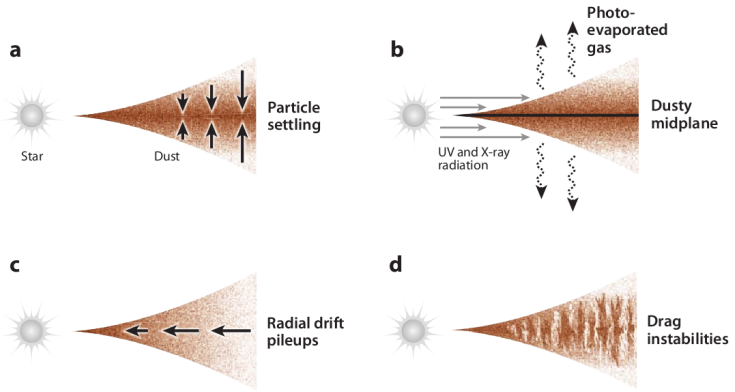


Figure 1: Four mechanisms for metal enrichment, none of which involving self-gravity (from [2]).

and as a consequence make it impossible to reach the density threshold presented in equation (2). An insight of what is the Kelvin-Helmholtz instability can be found in the Appendix A.

One can wonder if this physical and qualitative insight has any physical meaning, or in other words, at what point the layer becomes instable, and if it occurs before it's thin enough to reach the previously highlighted density thresholds. In order to tackle this point, let's rewrite these two conditions in terms of height of the layers. Be $H_g$ the total (half-)height of the gas, and $z_d$ the (half-)thickness of the dust. The two conditions reads:

$$(\frac{z_d}{H_g})_{Q<1} \leq 10^{-4}(\frac{r}{a.u.})^{\frac{3}{14}} \tag{4}$$

$$(\frac{z_d}{H_g})_{\text{KHI stable}} \geq 10^{-2}(\frac{r}{a.u.})^{\frac{2}{7}}) \tag{5}$$

Thus, the layer should become KH instable two orders of magnitude before it can collapse under the action of the collective gravity.

### *1.2. Dust and gas*

The differential rotation in the vertical direction arises because the dusty layer rotates at a different speed than the dust-free layer.

The dust-free layer (gas layer) revolves slightly slower than the Kepler velocity, because the pressure gradient in the radial direction supports the gas.

On the other hand, the dust particules don't feel this pressure support, and are assumed to rotate at the full Kepler velocity. Then, provided their stopping time[1] is small enough, they are well coupled to the fluid and *drag* the layer (dust + gas) revolve as a whole. The velocity is given by:

$$\Omega = \Omega_K(1 - \frac{\rho_g}{\rho_0}\eta) \tag{6}$$

The non dimensional parameter $\eta$ is a measure of centrifugal support by pressure:

$$\eta = \frac{-1}{2\rho_g\Omega_K^2 r}\frac{\partial P}{\partial r} \tag{7}$$

[1]The stopping time $\tau_s$ is one key parameter in the study of the growth of grains. It varies according to the size of the grains, and the radius, because different physical processes can dominate (Epstein regime, Stokes regime, etc.). A detailed study can be found in [10].

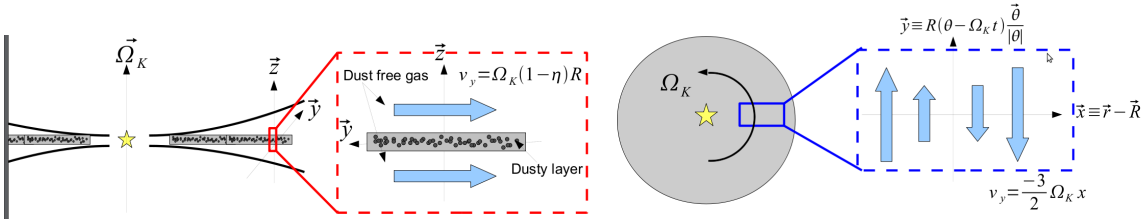


Figure 2: The local Cartesian coordinates system.

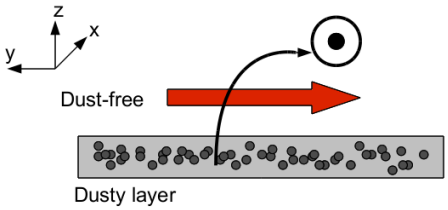


Figure 3: The action of the Coriolis force in the KHI context.

### *1.3. The KHI in rotating disks*

The picture drawn in the previous section is very general, but one has to take into account some refinements in order to try and answer to the problem. The main point is that the problem is not two dimensional, and the Coriolis force as well as the radial Keplerian shear play a critical role.

The local Cartesian coordinate system of interest is illustrated figure 2. It is a frame whose origin is at a radius $R$, and comoving at the local Keplerian speed around the star (eg. coupled with the dusty layer):

$$\mathbf{x} = \mathbf{r} - \mathbf{R} \tag{8}$$

$$\mathbf{y} = R[\Phi - \Omega t]\frac{\mathbf{\Phi}}{\Phi} \tag{9}$$

$$\mathbf{z} = \mathbf{z} \tag{10}$$

with $\mathbf{r}$, $\mathbf{\Phi}$ and $\mathbf{z}$ the usual cylindrical coordinates.

In this context of the KHI in a rotating frame, the Coriolis force becomes one central physical process. Indeed, and as pictured figure 3, it converts azimuthal motions excited by the KHI (the solid arrow in figure 3) to radial motions (the inward vector in the same figure). Then, the radial shear dissipates the non-axisymetric motions excited by the KHI by stretching them azimuthally (this is the qualitative picture, as the Keplerian shear rate is at least of the order of the Brunt-Visl frequency $|\frac{\partial\Omega_K}{\partial \ln r}| \gtrsim \omega_b$).

As a consequence, the conclusion to draw from this is that the Richardson number, though relevant in two dimensional common KHI, doesn't take into account all the physics at stake in the problem of growing grains through the Gravitational instability in dusty layers in protoplanetary disks. Thus, we shouldn't use the value of $Ri = \frac{1}{4}$ blindly.

This has been seen in simulations from [6] that the correct criteria for marginal stability is not a constant Richardson number, but depends linearly on $\mu_0$, the midplane dust to gas ratio.

$$\mu_0 = \frac{\rho_{dust}(0)}{\rho_{gas}} \tag{11}$$

This is represented figure 4, and is the very motivation for this project: can we explain this behavior through a semi-analytical model based on basic hydrodynamics.

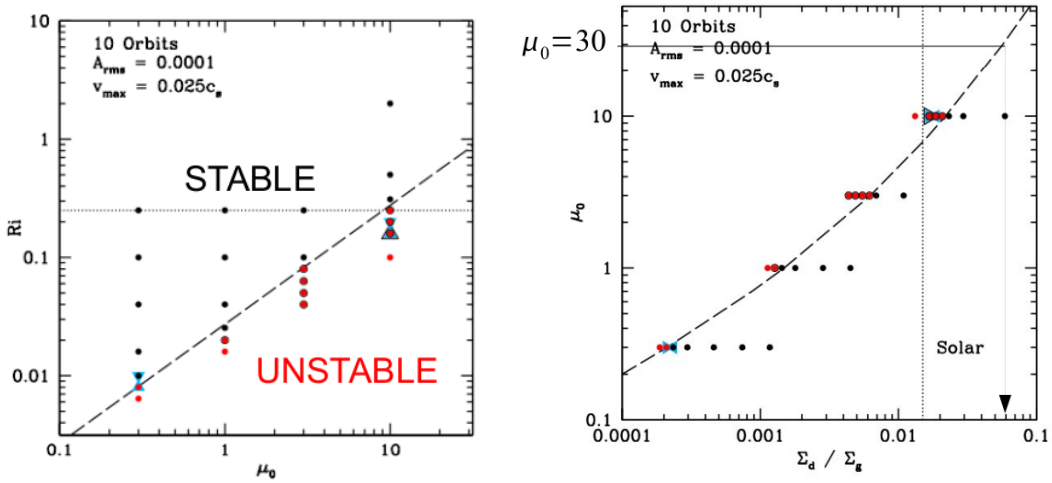


Figure 4: Several simulations (represented by black or red dots) of a 3D shearing box with Coriolis forces and tidal shear. Black dots correspond to stable runs, whereas red dots correspond to unstable runs. Left: Richardson number as a function of the metallicity, the dotted line corresponds to a fit of the marginally stable runs. Dotted line corresponds to $Ri = \frac{1}{4}$. Right: Same data, in a different parameter space, say metallicity in function of the bulk (height-integrated) dust-to-gas ratio. The dotted line corresponds to the solar bulk metallicity. These figures have been taken from [6], see their paper for a more precise explanation of the making off.

### *1.4. Further motivation*

The dependence of the stability on such parameters as the Richardson number and the metallicity (or equivalentlye, the dependence of the Richardson number on the metallicity for marginal stability), is very important in the context of planetesimal growth.

Indeed, according to equations (2) and (3), we need to achieve a density about 35 times greater than the mean disk density to trigger gravitational collapse.

$$\frac{\rho}{\rho_g} \gtrsim 35 \, (\frac{r}{a.u.})^{\frac{-3}{14}} \tag{12}$$

In the relevant parameter space, it means $\mu_0 \gtrsim 35$, and this is drawn on figure 4 on the right extrapolating the linear relation between the Richardson number and $\mu_0$ to higher metallicities. This leads to the bulk metallicity:

$$\frac{\Sigma_d}{\Sigma_g} \simeq 4 \times (\frac{\Sigma_d}{\Sigma_g})_{\text{solar}} \tag{13}$$

## 2. Method

### *2.1. Physically driven approximations*

This semi-analytical study is based on the work done by [5], who have performed a three-dimensional linear perturbation analysis in the context of protoplanetary disks.

We use the previously described local Cartesian coordinate system at a radius $R$ (see figure 2), rotating around the central star with the Kepler angular frequency $\Omega_K$:

$$\mathbf{x} = \mathbf{r} - \mathbf{R} \tag{14}$$

$$\mathbf{y} = R[\Phi - \Omega t]\frac{\mathbf{\Phi}}{\Phi} \tag{15}$$

$$\mathbf{z} = \mathbf{z} \tag{16}$$

We neglect self-gravity, but not the gravity of the central star, which leads to a radial force (competition between gravity of the star and the centrifugal force) and a vertical force (due to the vertical tidal gravity : $\Omega_K^2 z$.

We treat the dusty layer and the dust-free layer as a single (incompressible) fluid with different densities, respectively $\rho_d(z)$ and $\rho_g$.

This enables us to write the equations of hydrodynamics:

$$\nabla \cdot \mathbf{v} = 0 \tag{17}$$

$$\frac{\partial \rho}{\partial t} + \mathbf{v} \cdot \nabla \rho = 0 \tag{18}$$

$$\frac{\mathbf{v}}{\partial t} + (\mathbf{v} \cdot \nabla)\mathbf{v} = -\frac{1}{\rho}\nabla P - 2\Omega_K \times \mathbf{v} - \Omega_K^2 \mathbf{z} + 3\Omega_K^2 \mathbf{x} \tag{19}$$

In order to eliminate the Keplerian part of the velocity ($v_K = -\frac{3}{2}\Omega_K x$), we introduce the drift velocity relative to the Keplerian velocity:

$$\bar{v} = v - v_K \tag{20}$$

*2.2. Steady state*

As we want to do a linear perturbation analysis, we have to define the steady state.

We thus assume an unperturbed state steady and uniform in $x$ and $y$ directions:

$$\frac{\partial}{\partial t} = \frac{\partial}{\partial x} = \frac{\partial}{\partial y} = 0 \tag{21}$$

We assume an unperturbed velocity in the azimuthal direction ($y$ direction in the local coordinate system):

$$u_0 = w_0 = 0 \tag{22}$$

We then have from equations (17), (18) and (19):

$$\frac{1}{\rho_0}\frac{\partial P_0}{\partial x} = 2\Omega_K \bar{v_0} \tag{23}$$

$$\frac{1}{\rho_0}\frac{\partial P_0}{\partial z} = -\Omega_k^2 z \tag{24}$$

Given an initial density background $\rho_0(z) = \rho_d + \rho_g$, and $\eta$, we calculate the azimuthal velocity:

$$\bar{v_0} = -\frac{\rho_g}{rho_0}\eta r \Omega_k \tag{25}$$

*2.3. Linearization*

We now linearize the equations (17), (18) and (19). In order to perform the Fourier transform in $y$ and $x$ we introduce the shearing coordinate $y' = y + \frac{3}{2}\Omega_K x t$ (same idea as previously with $\bar{v}$). We assume that perturbed quantities (velocities, density and pressure) are written:

$$\tilde{f_1}(x, y, z, t) = f_1(z, t) e^{i(k_y y' + k_x x)} \tag{26}$$

where $f_1(z, t)$ is a complex function of $z$ and $t$.

The equations now read, with $k'_x = k_x + \frac{3}{2} k_y \Omega_K t$:

$$ik'_x u_1 + ik_y v_1 + \frac{\partial w_1}{\partial z} = 0 \tag{27}$$

$$\frac{\partial \rho_1}{\partial t} + ik_y \bar{v_0} \rho_1 = 0 \tag{28}$$

$$\frac{\partial u_1}{\partial t} + ik_y \bar{v_0} u_1 = -ik'_x \frac{P_1}{\rho_0} + 2\Omega_K \frac{\bar{v_0}}{\rho_0} \rho_1 + 2\Omega_K v_1 \tag{29}$$

$$\frac{\partial v_1}{\partial t} + ik_y \bar{v_0} v_1 = -ik_y \frac{P_1}{\rho_0} - \frac{d\bar{v_0}}{dz} w_1 + \frac{1}{2}\Omega_K u_1 \tag{30}$$

$$\frac{\partial w_1}{\partial t} + ik_y \bar{v_0} w_1 = \frac{-1}{\rho_0} \frac{\partial P_1}{\partial z} - \frac{\Omega_k^2 z}{\rho_0} \rho_1 \tag{31}$$

*2.4. Boundary conditions*

We consider solid-wall boundary condition at $z = 0$ (equatorial plane) and $z = z_0$ (the end of the box). We choose $z_0$ large enough so that the modes decay sufficiently when reaching this boundary (in practice, twice the height of the dusty layer seems to be enough). Thus, we have:

$$w_1 = 0 \quad \text{at } z = 0 \text{ and } z = z_0 \tag{32}$$

$$\frac{\partial P_1}{\partial z} + \Omega_K^2 z \rho_1 = 0 \quad \text{at } z = 0 \text{ and } z = z_0 \tag{33}$$

$$\frac{\partial \rho_1}{\partial z} + ik_y \bar{v_0} \rho_1 = 0 \quad \text{at } z = 0 \text{ and } z = z_0 \tag{34}$$

Adding another condition such as $\rho_1 = 0$ at $z = 0$ and $z = z_0$ for simplicity gives the final set:

$$\rho_1 = 0 \tag{35}$$

$$\frac{\partial P_1}{\partial z} = 0 \quad \text{at } z = 0 \text{ and } z = z_0 \tag{36}$$

*2.5. Initial density background*

The density profile we use is the same [6] used for their simulations. It has been derived by [8], based on the basic assumption of a constant Richardson number in the dust layer. Other profiles can be used (such as the one used in [5]), for example to compare and test our solutions.

The conditions $Ri =$ constant, $\frac{\partial \rho_g}{\partial z} << \frac{\partial \rho_d}{\partial z}$ and $g = -\Omega_K^2 z$ yield:

$$\rho_0 = \left[ \frac{1}{\left(\frac{1}{1+\mu_0}\right)^2 + \left(\frac{z}{z_d}\right)^2} \right]^{\frac{1}{2}} \tag{37}$$

where $\mu_0 = \frac{\rho_d}{\rho_g}$, is the initial dust-to-gas ration at the midplane, and

$$z_d = (Ri)^{\frac{1}{2}} \eta R \tag{38}$$

is a characteristic dust height. The dust density decreases from the midplane until it reaches zero at $z_{max}$:

$$|z_{max}| = \frac{\sqrt{\mu_0(2+\mu_0)}}{1+\mu_0} z_d \tag{39}$$

Figure 5 represents the density background (bottom) and the derived velocity background (top). The subscript 2 stands for the smooth background we used in our simulations, to get rid of the discontinuity of the first derivative of the density at the end of the dust layer (details can be found in **??**).

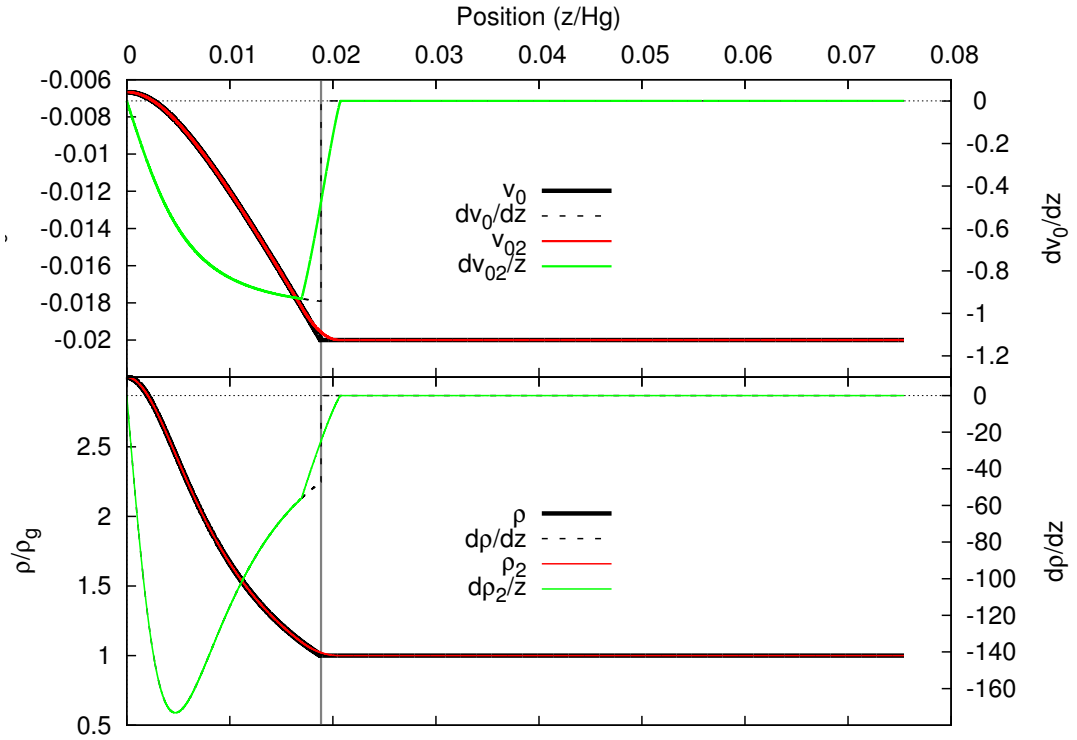


Figure 5: Top: velocity background $\bar{v_0}$. Bottom: density background $\rho_0 = \rho_g + \rho_d(z)$. The black and red solid lines represent respectively the raw (Sekiya's) background profiles and the smoothed ($C^1$ class) profile. The black dashed and green lines are the derivatives of respectively the raw (Sekiya's) profile, and the smoothed profile.

*2.6. Numerical method*

We follow the MAC method (Marker And Cell, [4]), where the pressure is determined by demanding that the continuity equation is satisfied at the next step. Any other quantity is then updated using this value.

We have:

$$\nabla \cdot \mathbf{v} = ik'_x u_1 + ik_y v_1 + \frac{\partial w_1}{\partial z} \tag{40}$$

Using: (29)$\times ik'_x$, (30)$\times ik_y$ and taking the partial derivative of (31) with respect to $z$, we obtain:

$$\begin{aligned}\frac{\partial(\nabla \cdot \mathbf{v})}{\partial t} =& - ik_y \bar{v_0}(\nabla \cdot \mathbf{v}) - 2ik_y \frac{d\bar{v_0}}{dz} w_1 - \frac{1}{\rho_0}\left(-k_x^{'2} - k_y^2 + \frac{\partial^2}{\partial z^2}\right) P_1 + \frac{1}{\rho_0^2}\frac{d\rho_0}{dz}\frac{\partial P_1}{\partial z} \\ &+ 2i\Omega_K k'_x \frac{\bar{v_0}}{\rho_0}\rho_1 + 2i\Omega_K k'_x v_1 + i\Omega_K k_y u_1 + \Omega_K^2 \frac{d}{dz}\left(-\frac{z}{\rho_0}\rho_1\right)\end{aligned} \tag{41}$$

Using first order approximation ($\frac{\partial(\nabla\cdot\mathbf{v})}{\partial t} \simeq \frac{(\nabla\cdot\mathbf{v})^{n+1} - (\nabla\cdot\mathbf{v})^n}{\Delta t} = \frac{-(\nabla\cdot\mathbf{v})^n}{\Delta t}$), we finally get:

$$\begin{aligned}\left(-k_x^{'2} - k_y^2 + \frac{\partial^2}{\partial z^2}\right) P_1^n = \rho_0 \Big\{ &\left((\Delta t)^{-1} - 2ik_y\bar{v_0}\right)(\nabla\cdot\mathbf{v})^n - 2ik_y\frac{d\bar{v_0}}{dz}w_1^n + 2i\Omega_K k_x^{'n} v_1^n \\ &+ i\Omega_K k_y u_1^n + 2i\Omega_K k_x^{'n}\frac{\bar{v_0}}{\rho_0}\rho_1^n + \Omega_K^2\frac{d}{dz}\left(-\frac{z}{\rho_0}\rho_1^n\right)\Big\}\end{aligned} \tag{42}$$

From this equation, we compute $P_1^n$, which we use to update every other quantity:

$$\rho_1^{n+1} = \rho_1^n + \Delta t\left\{-ik_y\bar{v_0}\rho_1^n - \frac{d\rho_0}{dz}w_1^n\right\} \tag{43}$$

$$u_1^{n+1} = u_1^n + \Delta t\left\{-ik_y\bar{v_0}u_1^n - ik_x^{'n}\frac{P_1^n}{\rho_0} + 2\Omega_K\frac{\bar{v_0}}{\rho_0}\rho_1^n + 2\Omega_K v_1^n\right\} \tag{44}$$

$$v_1^{n+1} = v_1^n + \Delta t\left\{-ik_y\bar{v_0}v_1^n - \frac{d\bar{v_0}}{dz}w_1^n - ik_y\frac{P_1^n}{\rho_0} + \frac{1}{2}\Omega_K v_1^n\right\} \tag{45}$$

$$w_1^{n+1} = w_1^n + \Delta t\left\{-ik_y\bar{v_0}w_1^n - \frac{1}{\rho_0}\frac{\partial P_1^n}{\partial z} - \frac{\Omega_K^2 z}{\rho_0}\rho_1\right\} \tag{46}$$

*2.7. Second order accuracy*

*2.7.1. In time*

In order to reach second order accuracy in time, we need to use a corrector-predictor as a method. To do this, we first replace *n-th* quantities on the right-hand side of equation (42) by:

$$f_1^{n+\frac{1}{2}} = \frac{f_1^{n+1} + f_1^n}{2} \tag{47}$$

We then solve for $P_1^{n+\frac{1}{2}}$.

Using now the quantities $f_1^{n+\frac{1}{2}}$, we compute the new and more accurate (up to the second-order) perturbed velocities and density (equations (43) to (46)):

$$f_1^{n+1} = f_1^n + \Delta t\{F_1^{n+\frac{1}{2}}\} \tag{48}$$

where $F_1^{n+\frac{1}{2}}$ stands for any variable expressed at time $n + \frac{1}{2}$.

*2.7.2. In space*

We use a discretized grid in $z$ of $N$ cells. Each quantity is defined at the grid points.

We have to solve at each time step equation (42), written as:

$$A_n X = B_n \tag{49}$$

where $A_n$ is an $N \times N$ tridiagonal (or band) matrix, X the vector ($X_i = P_1(i)$) to solve for, and $B_n$ is the right-hand side of the equation.

We use an $LU$ decomposition, which means that we don't explicitly solve for the inverse of A, but the solution X is a given function of $L_{ij}$ and $U_{ij}$. Writing everything (derivative) up to second order gives the following expression:

$$A_{i,i} = -[2 + (k_x^{'2} + k_y^2)(\Delta x)^2] \tag{50}$$

$$A_{i,i+1} = 1 - \frac{1}{2\rho_0(i)} \frac{d\rho_0(i)}{dz} \tag{51}$$

$$A_{i+1,i} = 1 + \frac{1}{2\rho_0(i)} \frac{d\rho_0(i)}{dz} \tag{52}$$

and the boundary conditions, given by using a ghost cell ($i = 0$ or $i = N + 1$) and enforcing $\frac{\partial P_1}{\partial z} = 0$ at the two borders[2]:

$$A_{1,2} = 2 \tag{53}$$

$$A_{N,N-1} = 2 \tag{54}$$

*2.8. Dimensionless quantities*

In order to work with dimensionless, order of unity equations, we use dimensionless variables by setting:

$$H_g = 1 \tag{55}$$

$$\Omega_K = 1 \tag{56}$$

$$\rho_g = 1 \tag{57}$$

$$c_s = 1 \tag{58}$$

We also define:

$$v_{max} = \eta R \Omega_K = \eta \frac{R}{H_g} c_s \tag{59}$$

Each simulation is then characterized by the choice of the density background, three free parameters $\left(Ri,\ \mu_0,\ \frac{v_{max}}{c_s}\right)$ and an initial perturbation ($u_1,\ v_1,\ w_1,\ \rho_1,\ P_1$).

## 3. Results

The goal is to sample the space parameter in $Ri$ versus $\mu_0$. To do this, we have chosen to use the value of the first peak after an exponential growth for a given perturbed quantity: $\rho_1$. An example of what it gives is shown figure 6, in the case $\mu_0 = 1$, and $v_{max} = 0.025$, for a bunch of different Richardson numbers.

The choice of the value of the first peak is motivated by its simplicity, and stability, contrary to an expected criteria for stability at very long time. In later studies, we seek for a better and more physically justified parameter to measure in the simulations.

[2]It then gives: $2P_1(1) - (2 + (k_x^{'2} + k_y^2)(\Delta x)^2)P_1(0) = (\Delta x)^2 \times \text{RHS}(i)$ at $z = 0$, and a similar expression at $z = z_{max}$.

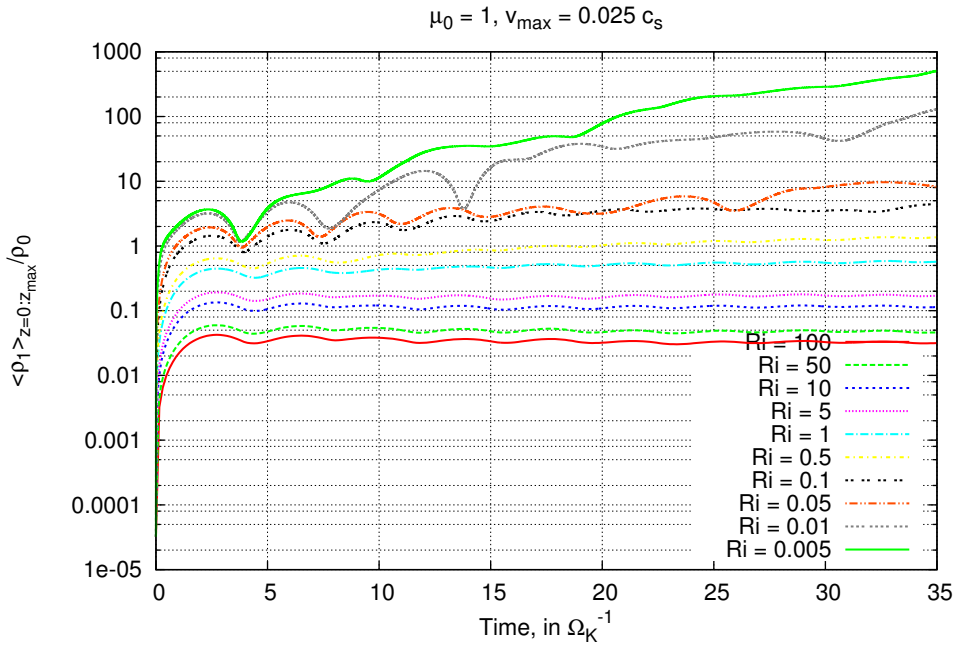


Figure 6: Example of the given run, at fixed $\mu_0 = 1$ and $v_{max} = 0.025$, for a bunch of Richardson numbers. The value of the first peak (at about $T = 3$) is used in further studies. The normalized value of $\rho_1$ is plotted in function of the number of Kepler times.

Because we carry out linear perturbation analysis, it's difficult to give a precise value for stability (or marginally stable runs). As a consequence, we don't give any typical value for stability, but we prefer to try and find *iso-stable* parameters. In detail, we use the raw value of the first peak in $\rho_1$, we normalize it to the initial total density $(\rho_g + \rho_d)$ at the midplane to have a scale-free value, and we then multiply it by the same total density to take into account the fact that we perturb the middle always with the same strength regardless of the density[3]. This is justified figure 7, where we plot two different runs with two different initial *kicks*.

### *3.1. Initial conditions*

To carry out a simulation, we need to specify the background, as highlighted previously, but also to give the initial perturbation. We first chose to study only odd modes in $w_1$, and then to choose any other quantity the most simple way. Thus, we choose $\rho_1 = u_1 = 0$, and $v_1$ is given by equation (27):

$$w_1 = C_{w1}(\sin(k_z z) + i\sin(k_z z)) \tag{60}$$

$$v_1 = C_{w1}\frac{k_z}{k_y}(-\cos(k_z z) + i\cos(k_z z)) \tag{61}$$

These initial conditions are then updated through the process we described in the previous section. Figure 8 shows two snapshots at $t = 0$ and a later ($t = 3\Omega_K^{-1}$) time.

### *3.2. The answer*

We now are ready to answer the initial question, by sampling the space $Ri/\mu_0$.

[3]A very dense midplane will be relatively less disturbed by the perturbation than a dust-free midplane.

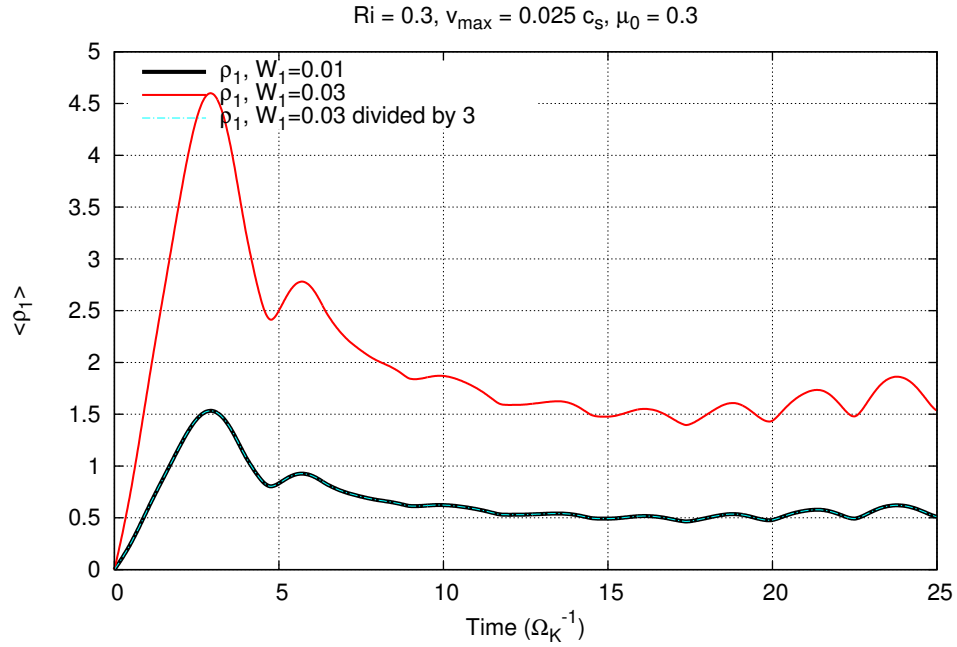


Figure 7: Two different runs (solid lines) with two different initial conditions (amplitude of the perturbation in $w_1$ different by a factor 3). The rescaled run (dashed, blue line) give exactly the same result as the original run (solid black line).

Figure 9 is the semi-analytical answer to figure 4 of [6]. What is important to notice is the dependence of $Ri$ with $\mu_0$ at low $\mu_0 < 10$, which confirms what has been seen in three-dimensional simulations by [6]. The behavior at larger metallicity ($\mu_0 > 10$) is qualitatively different: a constant Richardson number seems to be the right criteria to assess the stability of the layer. This doesn't contradict entirely previous simulations: the high-$\mu_0$ runs in [6] might not have reached convergence yet (blue triangles figure 4 are values for marginal stability with twice the resolution, and have lower critical Richardson number.

### *3.3. Another criteria ?*

This study supports the fact that the Richardson number is not the (only) relevant criteria to assess of the stability of the dust-rich midplane, as it had been foreseen by [6] and [1]. Following [6], we can try to derive a better fitted parameter, say the Shearing number, defined by analogy with the Richardson number as the square of the stabilizing effect (Kepler shearing frequency) over the vertical shearing rate:

$$Sh = \frac{|\frac{\partial \Omega_K}{\partial \ln r}|^2}{(\frac{\partial v_\phi}{\partial z})^2} \propto (\frac{\Delta z}{\Delta v_\phi})^2 \propto Ri \frac{1+\mu_0}{\mu_0} \tag{62}$$

If we assume that a marginally stable layer has a constant shearing number (we assume this number is the right criteria to use), then we get:

$$Ri_{crit} \propto \mu_0 \quad \text{for } \mu_0 << 1 \tag{63}$$

$$Ri_{crit} \sim \text{constant} \quad \text{for } \mu_0 \gtrsim 1 \tag{64}$$

and this is what is seen figure 9 !

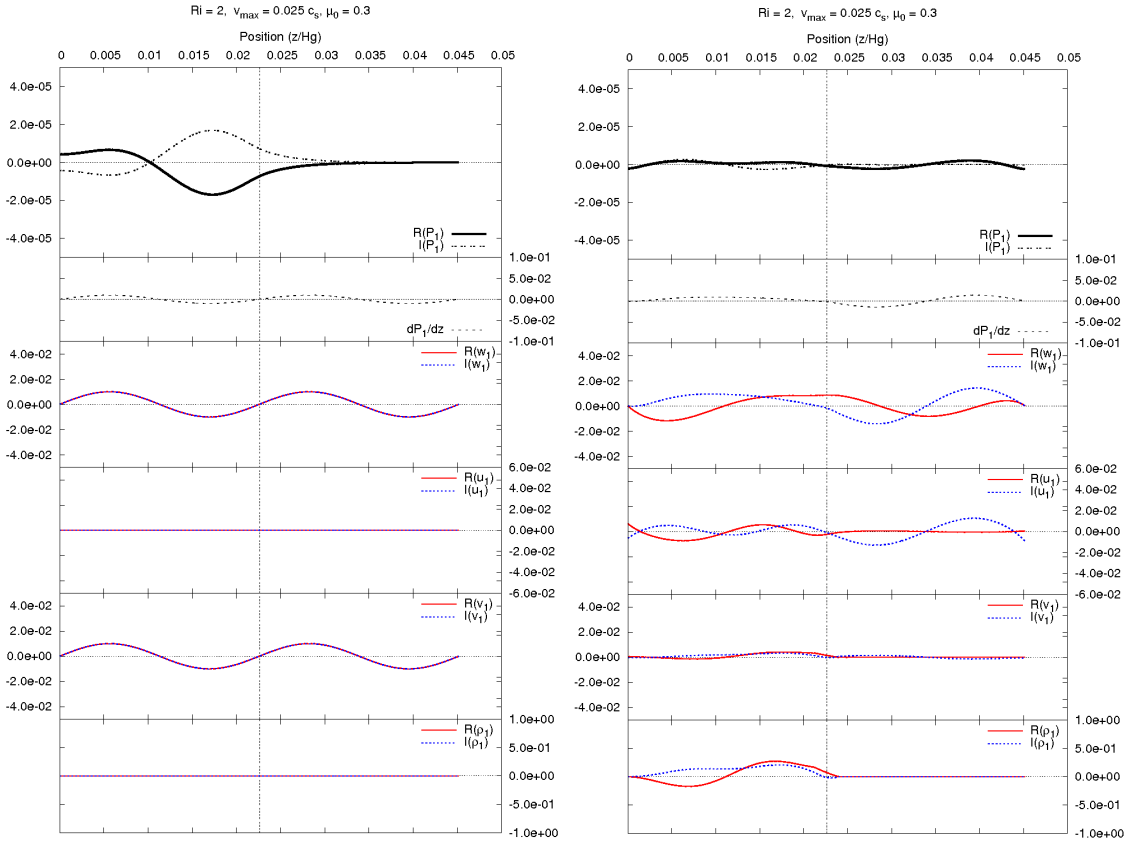


Figure 8: Solid lines represent the real part of each quantity, and dashed lines the imaginary part. Left: initial perturbation ($t = 0\Omega_K^{-1}$). Right: later time ($t = 3\Omega_K^{-1}$).

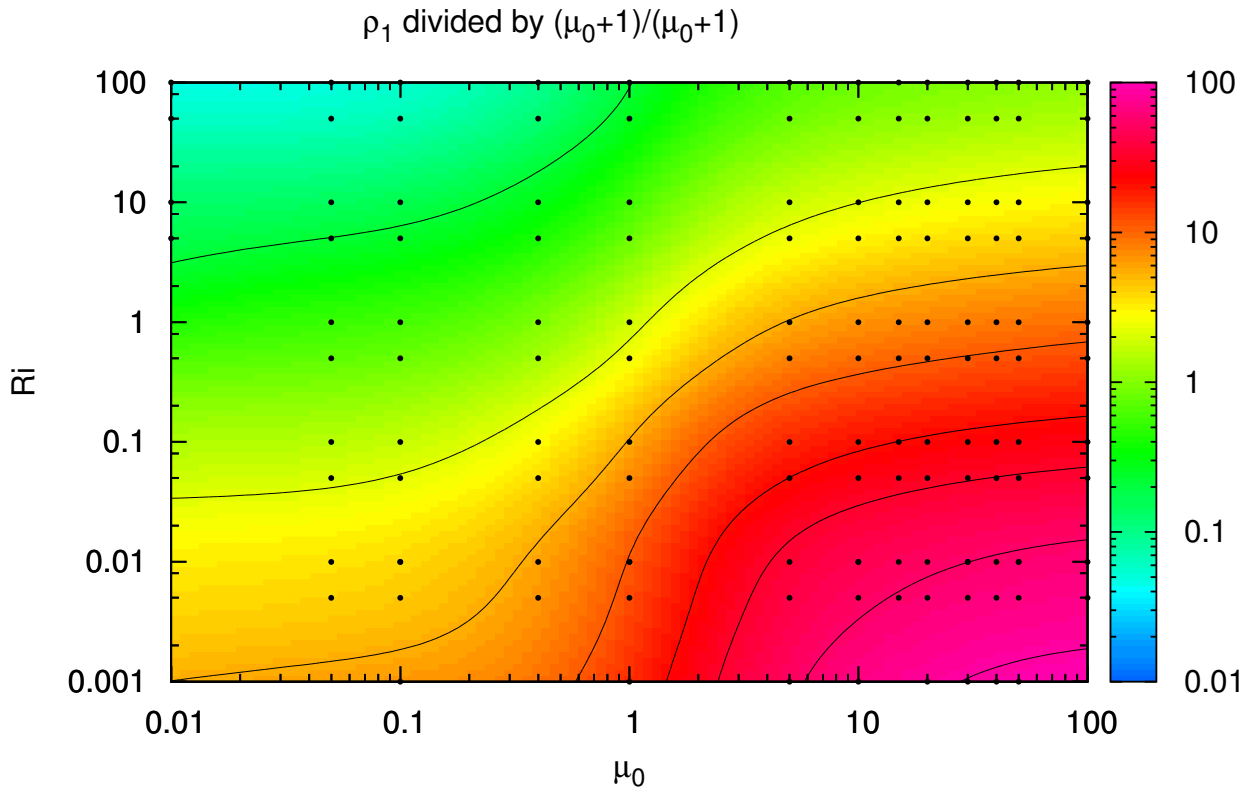


Figure 9: This plot is an extrapolation to the whole $Ri/\mu_0$ plane of several runs. Each dot represents a given simulation: $Ri$, $v_{max}$ and $\mu_0$, and then a value for $\rho_1$. The color-scale is the value of $\rho_1$ at the first peak, normalized and corrected according to the initial total density at the midplane. The isolines are drawn in solid black lines.

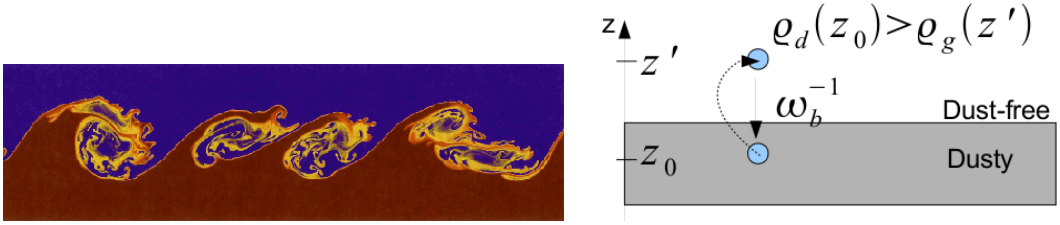


Figure A.10: Left: illustration of the Kelvin-Helmholtz instability in a numerical simulation. Right: illustration of the buoyancy, the stabilisation of two layers of different density against the shear.

## 4. Conclusions and work in progress

We have studied the stability of the equatorial, dust-rich midplane in protoplanetary disks, and found two trends. At low $\mu_0$, the critical Richardson number goes linearly with $\mu_0$, while at high $\mu_0$, the critical Richardson number is constant.

The underlying consequence of this result for the formation of planetesimals is that a constant Richardson number for high $\mu_0$ would lead to a requirement even lower than four times the solar nebula's bulk metallicity in order to trigger the gravitational instability in the dust-rich midplane (four times is what gives the linear fit on figures 4).

Achieving supersolar bulk metallicities can be done locally, for example through radial pileup ([11]). There are also other promising ways to achieve greater density (maybe up to the Toomre threshold !) with the streaming instability or turbulent concentration of particules, but they have not been studied here.

In the near future, we are going to continue this study, and try to represent in real coordinates the behavior of a particule (drawing the field lines).


## Acknowledgement

I want to thank Takayuki Muto and Eugene Chiang, my two advisors for the duration of the project, for all the work they have done and all the help they gave me. Also, Pascale Garaud and all the local team, for making this program possible.


## Appendix A. Kelvin-Helmholtz instability

The Kelvin-Helmholtz instability (hereafter KHI) occurs in parallel shear flows, and is not to be mistaken as turbulence. This instability is not only of interest in astrophysics, but in almost any hydrodynamical process : clouds in earth, flows in pipes, or the giant vortex in Saturn. Basically, it is a competition between a destabilization: the shear between the two fluids which tends to mix them in a single fluid; and a stabilisation: either the buoyancy (see figure A.10 on the right) in the classical KHI, or another stabilizing effect such as the Keplerian shear in other contexts.

A good indicator for the stability of the layers against the KHI is the squared ratio of the Brunt-$V\ddot{a}$isl frequency ($\omega_b = (\frac{g_z}{\rho}\frac{\partial \rho}{\partial z})^{\frac{1}{2}}$) over the shearing rate ($\omega_{shear} = \frac{dv_\phi}{dz}$): the Richardson number.

$$Ri = (\frac{\omega_b}{\omega_{shear}})^2 = \frac{\frac{g_z}{\rho}\frac{\partial \rho}{\partial z}}{(\frac{dv_\phi}{dz})^2} \tag{A.1}$$

For parallel two dimensional shear flows, the Richardson number is a good criteria to assess of the stability of the flows: the necessary condition for instability is $Ri < \frac{1}{4}$. Nevertheless for non parallel, three dimensional flows in a rotating frame, it is not obvious that the same criteria should apply !

## Appendix B. Smooth density background

Sekiya's ([8]) profile is discontinuous in the first derivative at the end of the dust layer. In order to make it continuous, with a Richardson number strictly increasing, various smoothing functions can be used. Two solutions based on powerlaws functions are implemented in the code.

The idea is to replace Sekiya's profile by a given function from a fixed height $z_l$ to $z_{up}$. We use the following function:

$$\tilde{\rho_0} = 1 + a(z_{up} - z)^b \tag{B.1}$$

keeping one over the three parameters ($a$, $z_{up}$, $b$) fixed. This function guaranties a strict decrease in $\rho_0$, and the needed boundary conditions at $z = z_{up}$:

$$\rho_0(z_{up}) = 1 \tag{B.2}$$
$$\partial_z \rho_0(z_{up}) = 0 \tag{B.3}$$

We can solve for the two free parameters, using the fact that $\frac{\rho_0 - 1}{\partial_z \rho_0} = \frac{z_{up} - z}{-b}$ and the given boundary conditions:

$$\rho_0(z_l) = \tilde{\rho_0}(z_l) \tag{B.4}$$
$$\partial_z \rho_0(z_l) = \partial_z \tilde{\rho_0}(z_l) \tag{B.5}$$

*Case 1: $z_{up} = z_l$ is fixed.* We have in that case:

$$b = \frac{(z_{up} - z_l)\rho_0^3}{(\rho_0 - 1)z_d^2} z_l \tag{B.6}$$
$$a = (\rho_0 - 1)(z_{up} - z_l)^{-b} \tag{B.7}$$

with $\rho_0 = \rho_0(z_l)$.

*Case 2: $b = 3$ is fixed.* In this case, the upper limit of the smoothing is not fixed. We now have:

$$z_{up} = \frac{3(\rho_0 - 1)z_d^2}{z_l \rho_0^3} + z_l \tag{B.8}$$
$$a = \frac{1 - \rho_0}{(z_l - z_{up})^3} \tag{B.9}$$

## References


[1] Chiang, E., Mar. 2008. Vertical Shearing Instabilities in Radially Shearing Disks: The Dustiest Layers of the Protoplanetary Nebula. Astrophys. J. 675, 1549–1558.

[2] Chiang, E., Youdin, A. N., May 2010. Forming Planetesimals in Solar and Extrasolar Nebulae. Annual Review of Earth and Planetary Sciences 38, 493–522.

[3] Goldreich, P., Ward, W. R., Aug. 1973. The Formation of Planetesimals. Astrophys. J. 183, 1051–1062.

[4] Harlow, F. H., Welch, J. E., Dec. 1965. Numerical Calculation of Time-Dependent Viscous Incompressible Flow of Fluid with Free Surface. Physics of Fluids 8, 2182–2189.

[5] Ishitsu, N., Sekiya, M., Sep. 2003. The effects of the tidal force on shear instabilities in the dust layer of the solar nebula. icarus 165, 181–194.

[6] Lee, A. T., Chiang, E., Asay-Davis, X., Barranco, J., Aug. 2010. Forming Planetesimals by Gravitational Instability. I. The Role of the Richardson Number in Triggering the Kelvin-Helmholtz Instability. Astrophys. J. 718, 1367–1377.

[7] Safronov, V. S., Zvjagina, E. V., Jan. 1969. Relative Sizes of the Largest Bodies during the Accumulation of Planets. icarus 10, 109–+.

[8] Sekiya, M., Jun. 1998. Quasi-Equilibrium Density Distributions of Small Dust Aggregations in the Solar Nebula. icarus 133, 298–309.

[9] Weidenschilling, S. J., Oct. 1980. Dust to planetesimals - Settling and coagulation in the solar nebula. icarus 44, 172–189.

[10] Youdin, A., Jul. 2008. From Grains to Planetesimals: Les Houches Lecture. ArXiv e-prints.

[11] Youdin, A. N., Shu, F. H., 2004. Planetesimal Formation by Gravitational Instability - The Goldreich-Ward Hypothesis Revisited. In: A. Penny (Ed.), Planetary Systems in the Universe. Vol. 202 of IAU Symposium. pp. 250–+.